Characteristics of Low-level Meso-γ-scale Vortices in the Warm Season over East China

Ying Tang[1,2,4], Xin Xu[1], Ming Xue[1,3], Jianping Tang[1], and Yuan Wang[1]

[1]Key Laboratory of Mesoscale Severe Weather/Ministry of Education, and School of Atmospheric Sciences, Nanjing University, Nanjing, Jiangsu 210023, P. R. China

[2]State Key Laboratory of Severe Weather,
Chinese Academy of Meteorological Sciences, Beijing 100081, P. R. China

[3]Center for Analysis and Prediction of Storms, and School of Meteorology,
University of Oklahoma, Norman, OK 73072, USA

[4]Shenzhen Meteorology Bureau, Shenzhen, Guangdong 518040, P. R. China

Corresponding to: Xin Xu (xinxu@nju.edu.cn)
Key Laboratory of Mesoscale Severe Weather/Ministry of Education,
School of Atmospheric Sciences, Nanjing University, Jiangsu 210023, China

Abstract

This work firstly studies the radar climatology of low-level meso-γ-scale vortices (MVs) occurred in the warm season of East China. Two kinds of MVs are considered which are, respectively, produced by isolated cells and mesoscale convective systems (MCSs). Results show that MVs most often occur in June and July. For MCS-type MVs, there is a high occurrence frequency in the late afternoon and early evening, while no apparent diurnal variation is found for cell-type ones. Moreover, MCS-type MVs tend to be stronger and longer-lived due to their favorable environment conditions of higher convective available potential energy (CAPE) and larger vertical wind shear. Compared to the supercell MVs in southeastern United States, the cell-type MVs in East China are much weaker and shorter-lived, indicating a lower occurrence frequency of supercells and thus prevailing of low-level MVs in East China than in the United States. The MCS-type MVs in East China mainly form in the developing and mature stages of their parent system which suggests that the cold-pool induced baroclinic vorticity plays a major role in the genesis of MV. This seems to be different from the MVs produced by quasi-linear convective systems (QLCSs) in the United States where frictional vorticity owing to surface drag contributes more significantly to MV genesis. Given their higher damaging potential, tracking of MVs within MCSs based upon the linear, least squares derivatives (LLSD) azimuthal shear used in this work would be helpful for the operational warning and forecasting of severe convective weather in East China.

Keywords: Meso-γ-scale vortices; convective systems; radar climatology; East China

1. Introduction

Convective systems can often produce severe weather like heavy rainfall, large hail, wind gusts, and downbursts (Burlando et al. 2012; Lompar et al. 2017; Abulikemu et al. 2016; Clavner et al., 2018). Strong rotating vortices of various horizontal scales are common characteristics of a number of severe weather systems, including tornadoes (from a few hundreds to a few thousands of meters), line-end vortices (several tens of kilometers), mesoscale convective vortex (MCV, about 200 km) and tropical cyclones (about 500–1000 km). At the meso-γ-scale (i.e., 2–20 km), there are two kinds of convective vortices, namely, mesocyclones within isolated convective storms such as supercells (Burgess et al. 1993) and mesovortices (Funk et al. 1999; Schenkman and Xue 2016) that are typically found in organized mesoscale convective systems (MCSs).

Mesocyclones are usually associated with deep and rotating updrafts of supercell thunderstorms. The rotation of midlevel mesocyclones is mainly caused by the tilting of horizontal vorticity associated with the ambient wind vertical shear. In contrast, the source of low-level rotation is believed to originate from the tilting of baroclinic horizontal vorticity generated at the cold-pool outflow boundary (Rotunno and Klemp 1985). Using 20 years of Doppler radar observations in Oklahoma, Burgess et al. (1993) found that about 30%~50% of mesocyclones can produce tornadoes. Trapp et al. (2005a) reassessed the percentage of tornadic mesocyclones based on a much larger set of radar data in the United States and found that the percentage of tornadic mesocyclones was only ~26%, lower than previously thought. According to 3 years radar data in Germany, Wapler et al. (2016) examined the characteristics of mesocyclones in Central Europe

which showed a prominent annual and diurnal cycles. Mesocyclones most often occur in the late afternoon and evening. Investigation of the relation between severe weather and mesocyclones showed that half of the hail events and all tornados were associated with a mesocyclone. The statistical features of mesocyclones in East China are similar to that in central Europe, as studied by Wang et al. (2018) using single Doppler radar observations from 2005 to 2013. They also found that high (low) centroid mesocyclones are favorable for the genesis of hailstorms (tornadoes).

Different from mesocyclones, mesovortices in general form on the leading line of quasi-linear convective systems (QLCSs, e.g., squall lines and bow echoes) below about 2–3 km (Funk et al. 1999; Atkins et al. 2004; Schenkman and Xue 2016). The structure and evolution of low-level mesovortices can also be simulated by convection-resolving models (Weisman and Trapp 2003; Ćurić et al. 2009; Schenkman et al. 2011). Based on idealized convection-resolving simulations, the formation of mesovortices had been attributed to either downward or upward tilting of baroclinic vorticity (Trapp and Weisman 2003; Atkins and Laurent 2009b). However, recent studies using real-data convection-resolving simulations that included surface friction revealed that the tilting of frictionally-generated horizontal vorticity owing to surface drag can also contribute to the vertical vorticity of mesovortices (Schenkman et al. 2012; Xu et al. 2015b; Schenkman and Xue 2016; Roberts and Xue 2017).

QLCS mesovortices are capable of producing tornadoes as well (Coniglio et al. 2010). As studied by Thompson et al. (2014), a larger percentage of QLCS tornadoes tend to occur in southeastern United States while more tornadoes over the central Great

Plains tend to be of supercell type. Radar-based analyses of mesovortices in a bow echo event in the United States suggested that tornadic mesovortices tended to be stronger, longer-lived, and deeper than their nontornadic counterparts (Atkins et al. 2004). Trapp et al. (2005b) studied the climatology of tornadoes spawned by QLCSs in the United States. Statistically, QLCS tornadoes were weaker than those produced by supercells. Both types of tornadoes showed a clear peak in occurrence near 1800 Local Standard Time (LST). However, QLCS tornadoes additionally displayed a higher occurrence frequency in the late night/early morning hours. QLCS tornadoes were also reported in Europe (e.g., Clark 2011; Gatzen 2011; Bech et al. 2015). According to their intensity distribution, Antonescu et al. (2016) argued that tornadoes were more likely spawned by QLCSs (supercells) over northern and southern (western and eastern) Europe.

Moreover, low-level mesovortices are closely related to damaging winds produced by QLCSs at the surface (Weisman and Trapp 2003). The presence of mesovortices can notably modify the outflow of QLCSs and hence affect the location of wind damages (Atkins et al. 2005). Generally, the strongest winds occur on the side of mesovortices where the mean translational flow and the vortex rotational flow are in the same direction. The vortical flow of mesovortices can account for up to 50% of the total wind (Atkins and Laurent 2009a; Xu et al. 2015a).

Recently, Davis and Parker (2014) studied the climatology of meso-γ-scale vortices (MVs) that occurred in the high-shear and low-CAPE environment of mid-Atlantic and southeastern United States using Doppler radar observations. Significant differences were found in the low-level azimuthal shear of MVs that can be used to discriminate

tornadic and nontornadic vortices. The MVs produced within supercells were found to be longer-lived than nonsupercell (mainly QLCSs) ones, with the latter of greater diameters and stronger intensities.

Convective systems are common in the warm season of East China. Many previous studies in this region had focused on larger-scale convective vortices such as MCV and the MCSs themselves (e.g., Meng et al. 2013; Zheng et al. 2013; He et al. 2017). There have been few studies on MVs in China, however, such that their spatial and temporal distributions and characteristics are still poorly understood. This work, for the first time, attempts to study the climatology of MVs in China by using multi-year Doppler radar observations. The main purpose is to improve our understanding on the characteristics (e.g., spatiotemporal distributions, intensity, size and duration) of MVs in East China, in particular of MVs that occur within MCSs. Because MVs are often accompanied by severe weather, including high winds, short-time intense rainfall or even tornadoes, the radar climatology of MVs presented herein can help forecasters better monitor severe convective weather and forecast their damaging potential. It can also benefit the study on climate trend of extreme weather events.

The remainder of this paper is organized as follows. Section 2 describes the dataset and methods utilized for detecting MCS and MV. Section 3 presents the radar climatology of MCSs and MVs in East China during the warm season of 2013–2015, together with their environment conditions. Finally, the paper is summarized in section 4 with additional discussions.

2. Data and methods

2.1. Data

In this work, three-year (2013–2015) Doppler radar observations from April to July at 17 radar sites are used, with their locations shown in Fig. 1a. In general, these radars cover the Yangtze and Huai River Basins (YHRB) between about 112–124°E and 28–36°N. The raw radar data are processed using the 88D2ARPS program of the Advanced Regional Prediction System (APRS, Xue et al. 2000) developed at the Center for Analysis and Prediction of Storms (CAPS), the University of Oklahoma. Firstly, data quality control is performed including the removal of non-meteorological echoes and de-aliasing of radial velocity (Brewster et al. 2005). The processed radar data are used for detecting MCSs and MVs and producing climatological statistics.

To investigate the environmental conditions of MCSs and MVs, the 6-hourly, 0.5°×0.5° National Centers for Environmental Prediction (NCEP) Global Forecast System (GFS) analyses are used.

2.2. Detection of MCS

The detection of MCS uses the mosaic of composite (i.e., column maximum) reflectivity of the 17 radars in YHRB, as produced by radar mosaic program RADMOSAIC from the ARPS system. The horizontal resolution of the radar mosaic reflectivity is 4 km, which is sufficient to capture MCSs. Given the time differences among the radar volume scans, the composite reflectivity mosaics are produced every 10 minutes.

According to the American Meteorology Society (AMS) Glossary (Glickman and

Zenk 2000), an MCS is defined as "… *a cloud system that occurs in connection with an ensemble of thunderstorms and produces a continuous precipitation area of the order of 100 km or more in horizontal scale in at least one direction* …" For the detection of MCSs, there are indeed many different criteria in literature. For example, Parker and Johnson (2000) defined an MCS as "(a) band of contiguous or quasi-contiguous larger than 40 dBZ ≥ 100km and lasting ≥ 3h, and (b) linear or quasi-linear convective area sharing a common leading edge." Herein, an MCS is defined as a continuous band of 35dBZ reflectivity extending at least 100 km in at least one direction and persisting for at least 2 hours, with a minimal area of 1000 km^2. This definition is similar to those used in previous studies of MCSs in East China (Meng and Zhang 2012; Zheng et al. 2013).

An objective detection procedure is proposed according to the definition above. Firstly, the composite reflectivity is smoothed using a 3×3 median filter as in Smith and Elmore (2004), in order to remove small-scale signals and thus better detect mesoscale systems. Secondly, convective bands of 35-dBZ are identified by an image recognition technique (Comaniciu et al. 2003). Thirdly, convective bands greater than 1000 km^2 are fitted by an ellipse to obtain their geometric features, e.g., orientation, eccentricity, and long axis (Gander et al. 1994). Only convective bands with an axis longer than 100 km will be considered as a potential MCS. Lastly, potential MCSs are tracked to obtain their lifetime to ensure that MCSs persist for at least two hours. There are a number of MCS tracking methods. In this study, the Maximum Spatial Correlation Tracking Technique (MASCOTTE) developed by Carvalho and Jones (2001) is used, which is

simple and effective for predicting and tracking the evolution of MCSs. This method is mainly based on the magnitudes of spatial correlation between two identified convective systems at successive times. The technique can provide several structural properties of the convective systems such as horizontal area, perimeter, and center of mass. Readers are referred to their paper for more details.

2.3. Detection of MV

Traditionally, meso-γ-scale, or even smaller-scale circulations (e.g., tornadoes) are detected by calculating the difference between radar radial velocities of adjacent azimuths at a given range (Mitchell et al. 1998). In the case of strong background winds, however, the difference between outbound and inbound velocities may become too weak. Moreover, the "gate-to-gate" azimuthal shear is not tolerant of radar data noise since the shear estimation relies only on two adjacent radial velocities. Herein, the linear least squares derivatives (LLSD) method developed by Smith and Elmore (2004) is adopted, which had been used by Davis and Parker (2014) and Xu et al. (2015a). At a given radar gate location, radial velocity is locally fitted by linear combination of azimuthal shear and radial shear of radial velocities at a number of gates. Therefore, the linearly regressed azimuthal shear is more tolerant of radial velocity noise.

As MVs generally occur at the low levels, only LLSD azimuthal shear at 0.5° elevation and within 150 km of the radar site is calculated. Beyond this distance, the radar azimuthal resolution becomes low and unsuitable for the detection of meso-γ-scale vortices. MVs are identified when the shear intensity exceeds 10^{-3} s^{-1}, that is, one order greater than the Coriolis parameter in midlatitudes. This intensity threshold is

smaller than that used in Davis and Parker (2014) because they aimed to study tornadic/ nontornadic vortices. Moreover, MVs should persist for at least 3 consecutive volume scans (about 18 minutes) of the operational weather radar. As such, MVs are tracked both backward and forward to obtain their lifetime, using an objective tracking method similar to the WSR-88D Storm Cell Identification and Tracking (SCIT) algorithm (Johnson et al. 1998).

MVs should be detected for each radar because the radial velocity cannot be composited for multiple radars. However, given the dense radar coverage in YHRB, the same MV might be detected by several radars simultaneously, leading to the problem of multiple counting. For this reason, MVs are only detected using data of three radars, i.e., the Wuhan, Hefei, and Yancheng radars, that are located in the upper, middle and lower reaches of YHRB, respectively (Fig. 1b). Together, these radars provide a good overall coverage of YHRB.

3. Results

3.1. Characteristics of MCSs

Figure 2 displays the spatial distribution of MCSs in YHRB. There are in total 95 MCSs from April to July of 2013 through 2015. Most MCSs formed in eastern Hubei and western Anhui province, i.e., the upper reach of YHRB. There are also a number of MCSs that are generated in northern Anhui and the adjacent Jiangsu province. After formation MCSs mostly move northeastward (not shown). Therefore, the three radars chosen for the examination of MVs are in the main path of MCSs in this region. It is

noteworthy that MCSs can also form in the Sichuan Basin (i.e., upstream of YHRB) and move eastward into YHRB. However, these MCSs are outside of our radar coverage.

The monthly variation of detected MCSs is shown in Fig. 3a. More than 60% of the MCSs take place in June and July, i.e., the YHRB rainy season. From middle/late June to early/middle July, a quasi-stationary, persistent Meiyu front often occurs in YHRB under the influence of Asian summer monsoon. MCSs are repeatedly generated and move along the Meiyu front, producing heavy rainfall (e.g., Xu et al. 2017). In contrast, there are fewer MCSs in April and May when the summer monsoon has not yet reached YHRB. Figure 3b displays the diurnal variation of MCSs in YHRB. MCSs most often occur in late afternoon through midnight, i.e., between 1500 and 0000 LST. A second peak is found in the early morning between 0600 and 0900 LST, likely related to early morning precipitation peak of Meiyu system owing to boundary layer inertial oscillations (Xue et al. 2018). The diurnal variations of MCSs are consistent with the findings of Meng et al. (2012).

3.2. Characteristics of MVs

With the three radars, there are 3790 MVs detected from April to July of 2013 through 2015. As shown in Table 1, about 50% of the MVs are detected by Hefei radar in the middle reach of YHRB. In comparison, only about 30% and 20% MVs occurred in the upper (Wuhan radar) and lower (Yancheng radar) reaches of YHRB, respectively. Figure 4 shows the spatial distribution of MVs. For the Wuhan and Hefei radar coverage regions, MVs are mainly distributed in the southwest and northeast quadrants of the

radar (Figs. 4a, 4b). For the Yancheng radar region, MVs are generally located on the left side when facing northeast (Fig. 4c). Given the geographic locations of the three radars, MVs tend to occur in an elongated region extending northeastward from eastern Hubei to northern Jiangsu province.

MVs exhibit greater monthly variation than MCSs. As shown in Fig. 5a, 45% of the MVs occur in July and 25% in June, with similar occurrence frequencies in April (14%) and May (16%). On the contrary, the diurnal variation of MVs is not as prominent as that of MCSs (Fig. 5b). MVs occur a little more frequently in the evening (1800 to 2100 LST) and early morning (0600 to 0900 LST), with a somewhat lower frequency between 0300 and 0600 LST. Such diurnal cycle is much weaker than that of mesocyclones/tornadoes in the United States and Europe (Trapp et al. 2005b; Dotzek 2001; Wapler et al. 2016). Figure 5c and 5d show the distributions of MV maximum size and shear intensity during their lifetime. Most MVs (about 70%) have maximum diameters between 4 km and 10 km, while only about 23% of MVs can grow larger than 10 km. For all MVs, the maximum diameter is 8.1 km on average (Table 2). As for the peak LLSD azimuthal shear representing the MV intensity, more than 80% of them are weaker than 3×10^{-3} s^{-1} (Fig. 5d), with a mean value of 2.3×10^{-3} s^{-1} (Table 2). As noted in section 2.3, the mean azimuthal shear of MVs in this work is lower than that documented in Davis and Parker (2014) for MVs in the United States.

The lifetime of MVs in YHRB is also examined. On average, the detected MVs persist for ~26.3 minutes (Table 2). This is comparable to the lifetime of nonsupercell vortices but shorter than that of supercell vortices found in southeastern United States

(Davis and Parker 2014). Based on the lifetime, MVs are divided into three subsets, i.e., short-lived (18–30 min), moderate-lived (30–60 min) and long-lived (> 60 min). Most MVs (69%) are short-lived, while only about 5% of MVs can persist for over an hour (Table 1). For the three sets of MVs, the monthly variations are similar to that of all MVs (Fig. 5a), although long-lived MVs have slightly higher occurrence frequencies in June and July (not shown). The diurnal variations of short- and moderate-lived MVs agree with that of all MVs. However, long-lived MVs have stronger diurnal variation, with higher frequencies in early afternoon, evening and early morning but very low frequency between 0000 and 0600 LST (not shown). Besides, long-lived MVs tend to have greater diameters and stronger azimuthal shears (Fig. 6). For instance, the maximum diameter of long-lived MVs is 10.2 km on average, which is 34% and 11% larger than those of short- and moderate-lived MVs, respectively (Table 2).

As mentioned in Introduction, MVs can be divided into two categories according to their parent system, i.e., cell- and MCS-type MVs. Seen from Table 1, there are 374 MVs spawn by MCSs, accounting for about 10% of the total MVs. This is qualitatively similar to the results of Trapp et al. (2005b) that in the United States about 79% (18%) of tornadoes were produced by storm cells (QLCSs). Nearly all MCS-type MVs occur in the middle and lower reaches of YHRB (i.e., with coverages of Hefei and Yancheng radars), although a considerable number of MCSs formed in the upper reach of YHRB (Fig. 2). This is because MVs are often generated in the developing and mature stages of MCSs (Fig. 7) when the system cold pool is well established, producing sufficient baroclinic vorticity for the genesis of low-level vertical rotation (Trapp and Weisman

2003; Atkins and Laurent 2009b). The MCSs that occurred in the eastern Hubei province are in their early stage of development and usually move quickly out of the detection range of Wuhan radar.

The MCS-type MVs are of greater monthly variations than cell-type ones (Fig. 8a). More than 60% of MCS-type MVs are found in July while only about 5% occur in May. They occur more than twice as frequently (~25%) between 1800 to 2100 LST than all other time periods of the day, which have similar percentages of occurrence of about 10% (Fig. 8b). Contrastingly, cell-type MVs have little diurnal cycle. This again differs from the diurnal cycle of cell-type tornadoes in the United States which have a clear peak in occurrence near 1800 LST (Trapp et al. 2005b).

The distributions of maximum diameter for the two types of MVs are shown in Fig. 8c. Cell-type MVs are in general smaller than 8 km, with a mean diameter of 6 km (Table 2). The maximum diameter of MCS-type MVs is concentrated in the range of 6 to 12 km, with a mean diameter of 10 km. Similarly, Fig. 8d displays the distribution of MV intensity in terms of maximum azimuthal shear. For both types, the azimuthal shear with the highest frequency is smaller than 2×10^{-3} s^{-1}, especially for cell-type MVs. On average, the maximum azimuthal shear of MCS-type MVs is 2.5×10^{-3} s^{-1}, which is about 20% larger than that of cell-type MVs (Table 2).

There are also distinct differences between the lifetimes of cell- and MCS-type MVs. Almost all MCS-type MVs persist for more than 30 minutes, while there are only about 8% for cell-type MVs (not shown). The mean lifetime of MCS-type MVs is about 46.4 minutes, nearly twice that of cell-type (Table 2). In particular, about 16% of the

MCS-type MVs last for more than an hour, with a mean lifetime of about 72 minutes (Table 3). These MVs are obviously long-lived MVs. For other shorter-lived MCS-type MVs, their mean lifetime is about 42 minutes. Long-lived MCS-type MVs tend to have higher intensities. The peak azimuthal shear is 3.2×10^{-3} s^{-1} on average, which is about 40% stronger than that of short-lived ones. The maximum diameters of the two subsets of MCS-type MVs are quite similar, however.

Davis and Parker (2014) studied the characteristics of MVs in southeastern United States. Their results showed that QLCS MVs were generally larger and stronger than supercell ones, consistent with our findings with MVs in YHRB. On the contrary, supercell MVs tended to be longer-lived than those produced by QLCSs, which differs from our findings with cell-type MVs. This is likely due to the fact that strong supercells are much less frequent in eastern China than in the United States, and many of the cells in our statistics are weaker and smaller ones. As for tornadoes that are smaller in scale than MVs, it is noteworthy that QLCS tornadoes are statistically weaker than supercell ones in the United States (Trapp et al. 2005b).

3.3. Composite synoptic conditions

Undoubtedly, the monthly variations of MCSs and MVs are affected by the monthly variations of synoptic conditions. Figure 9 shows the composite environmental conditions in East Asia during 2013–2015. In April and May (Figs. 9a, 9b), an intense upper-level jet of over 40 m s^{-1} is present at 200 hPa. YHRB is at the entrance region of the upper-level jet. At 500 hPa, the subtropical high is located south of 20°N, with

YHRB located underneath broad westerlies in midlatitudes. At 850 hPa, a trough stretches from Northeast China to the Yellow Sea. Northwesterly winds behind the trough and southwesterlies associated with the subtropical high are found to converge in YHRB. In June and July (Figs. 9c, 9d), the upper-level jet is weakened and shifted northward and westward. YHRB is now on the southern flank of the jet exit region where the ascending branch of the jet-induced secondary circulation is found. At 500 hPa, the midlatitudes of East Asia are dominated by westerlies, featuring weak temperature advection. The subtropical high has moved northward to about 25°N and retrogressed eastward to the Northwest Pacific. As a result, southern YHRB is under the influence of southwest flows along the western periphery of subtropical high. In the lower troposphere, due to the northward progression of Asian summer monsoon, much more warm, moist air of high equivalent potential temperature (θ_e) is transported to YHRB from South China Sea and Indian Ocean than in April and May.

Figure 10 depicts the spatial distributions of CAPE and vertical wind shear between 1000 and 700 hPa. Benefiting from the transport of high-θ_e air by the monsoonal flow, the CAPE over YHRB is notably increased in June and July (Figs. 10a, 10c). The mean CAPE is 386 J kg^{-1}, which is ten times greater than that of April and May (Table 4). In both periods, the vertical shear in the layer of 1000–700 hPa is approximately toward east in YHRB, with stronger shear found in eastern YHRB (Figs. 10b, 10d). Overall, the low-level vertical shear is stronger in April and May (5.7 m s^{-1}) than in June and July (4.3 m s^{-1}). The relatively weak shear in the warm season of YHRB is thus not favorable for supercell storms.

Synoptic conditions for the cell- and MCS-type MVs in YHRB are also studied. As shown in Fig. 9e, for cell-type MVs, there is weak synoptic-scale forcing in the middle troposphere, with predominantly zonal winds over YHRB. At 200 hPa, a west-east oriented jet streak is located just north of YHRB. In the case of MCS-type MVs (Fig. 9g), the 200-hPa jet breaks into two segments over East Asia. The eastern jet, with the jet core located northeast of YHRB, is more intense compared to the case of cell-type MVs. YHRB is located to the right of the jet entrance region, where rising motion due to synoptic-scale secondary circulation is expected. At 500 hPa, there exists a short-wave trough which can increase the temperature advection over YHRB. In the lower troposphere (Figs. 9f, 9h), YHRB is under the influence of synoptic-scale southwesterly flows extending from Indian Ocean to the Northwest Pacific. In the case of MCS-type MVs (Fig. 9h), the southwesterly flows are much stronger, forming a low-level jet (LLJ) at the 850 hPa level. A closed cyclonic circulation is found in YHRB, on a shear line (between the southwesterly flows from the south and northeasterly flows from the north) that typically exists in the region during the warm season. Positive vertical vorticity in the region favors the development of convective systems. Due to the LLJ, there is more water vapor flux into YHRB, giving rise to greater CAPE than in the case of cell-type MVs (Figs. 10e and 10g, see also Table 4). The presence of LLJ also enhances the low-level vertical shear which can be greater than 12 m s^{-1} (Fig. 10h). Therefore, compared to the cell-type MVs, MCS-type MVs are mainly generated in an environment of higher CAPE and stronger low-level vertical shear.

4. Conclusions

This work focuses on the radar-based climatology of meso-γ-scale vortices (MVs) occurred in the warm season of East China, and in particular, in the Yangtze-Huai River Basins (YHRB). As a first study of this kind, detailed characteristics and environment conditions are examined for two kinds of MVs that are produced by isolated cells and mesoscale convective systems (MCSs), respectively. Features of MVs in East China are also compared to those of MVs in other countries, especially the United States.

In the period of April to July of 2013–2015, there are 3790 MVs detected in YHRB, about 10% of which are produced by MCSs. The majority of MVs (~70%) occurred in June and July, i.e., in the rainy season of YHRB. MVs more often formed in the evening and early morning, with a low occurrence frequency at night. In general, MVs are short lived (< 30 minutes), while only about 5% can persist for over 60 minutes.

Notable differences are found between the two kinds of MVs. MCS-type MVs most often occur in the late afternoon and early evening. On the contrary, there is no apparent diurnal variation for cell-type MVs. Overall, MCS-type MVs tend to be larger, stronger and longer-lived than cell-type ones. Examination of ambient conditions reveals that MCS-type MVs generally occur in an environment of stronger upper and middle level synoptic forcings. A southwesterly jet is present in the low level which transports more warm and moist air into YHRB, leading to higher CAPE and stronger low-level shear that favor the development of strong and long-lived MVs (Weisman and Trapp 2003; Atkins and Laurent 2009b).

Compared to the cell-type MVs in East China, the MVs produced by supercells in southeastern United States are significantly longer-lived (Davis and Parker 2014). The

supercell MVs are also longer-lived (and stronger) than those generated within QLCSs, which is opposed to the case of cell- and MCS-type MVs in East China. This indicates that the isolated cells in East China are prone to be weaker than their US counterparts, i.e., they are more likely to be ordinary cells rather than supercells. The fact that East China has less frequent supercells can be readily inferred from the weak CAPE (< 600 J kg^{-1}) and ambient vertical shear (< 10 m s^{-1}), both of which are unfavorable for the development of supercelluar storms. As a result, it can be concluded that low-level MVs prevail in East China compared to the United States.

Moreover, the MCS-type MVs in East China mainly formed during the developing and mature stages of their parent convective systems. This suggests that the baroclinic horizontal vorticity produced by system cold pool is of great importance for the genesis of low-level MVs. This finding appears to be different from the case of QLCS MVs in the United States——surface friction was found to play an important role in producing the MVs (Schenkman et al. 2012; Xu et al. 2015b). Nonetheless, to better understand the dynamics of MVs occurred in the typical environment of East China, both idealized and real-data numerical simulations as well as sensitivity experiments are still needed, which will be addressed in the future research.

Finally, although accounting for only a small fraction of total MVs in East China, MCS-type MVs may induce more severe weather hazards, given their strong intensity and long-lasting lifetime compared to their cell-type counterparts. For instance, a cruise ship capsized in Yangtze River on 1 June 2016, leading to over 400 fatalities (Meng et al. 2016). This shipwreck was attributed to the high straight-line winds near the apex

of a bow echo, which were likely produced by low-level MVs formed on the leading edge of the bow echo (Xu et al. 2015a; Atkins and Laurent 2009a). In view of their damaging potential, tracking of MVs within MCSs (probably based on the LLSD azimuth shear of radial velocity as in this research) should be of practical use for the operational warning and forecasting of severe convective weather. Towards that end, it is thus necessary to further explore the relation between MVs and severe weather hazards according to more observations (e.g., automated surface stations, and severe weather report), in parallel with development of advanced MV detection and tracking technique.

Acknowledgments. The authors would like to thank the anonymous reviewers for their constructive comments. This study was mainly supported by the National Key R&D Program of China (2018YFC1507303), National Science Foundation of China (Grants 41875068, 41505046, and 41750965), Fundamental Research Program of Chinese Academy of Meteorological Sciences (2017Z017, Grant 2017LASW-A02), and the Fundamental Research Funds for the Central Universities (0207-14380046).

References

Abulikemu, A., Xu X., Wang Y., Ding J.F., Zhang S.S., Shen W.Q., 2016. A modeling study of convection initiation prior to the merger of a sea-breeze front and a gust front. Atmos. Res., 182, 10–19. https://doi.org/ 10.1016/j.atmosres.2016.07.003

Antonescu, B., Schultz, D.M., Lomas, F., 2016. Tornadoes in Europe: synthesis of the

observational datasets. Mon. Weather Rev., 44, 2445–2480. https://doi.org/10.1175/MWR-D-15-0298.1

Atkins, N.T., St. Laurent, M., 2009a. Bow echo mesovortices. Part I: Processes that influence their damaging potential. Mon. Weather Rev., 137, 1497–1513. https://doi.org/10.1175/2008MWR2649.1

Atkins, N.T., St. Laurent, M., 2009b. Bow echo mesovortices. Part II: Their genesis. Mon. Weather Rev., 137, 1514–1532. https://doi.org/10.1175/2008MWR2650.1

Atkins, N.T., Arnott, J.M., Przybylinski, R.W., Wolf, R.A., Ketcham, B.D., 2004. Vortex structure and evolution within bow echoes. Part I: single-doppler and damage analysis of the 29 June 1998 derecho. Mon. Weather Rev., 132, 2224–2242. https://doi.org/10.1175/1520-0493(2004)132<2224:VSAEWB>2.0.CO;2

Atkins, N.T., Bouchard, C.S., Przybylinski, R.W., Trapp R.J., Schmocker, G., 2005. Damaging surface wind mechanism within the 10 June 2003 Saint Louis bow echo during BAMEX. Mon. Weather Rev., 133, 2275–2296. https://doi.org/10.1175/MWR2973.1

Bech, J., Arús, J., Castán, S., Pineda, N., Rigo, T., Montanyà, J., van der Velde, O., 2015. A study of the 21 march 2012 tornadic quasi linear convective system in Catalonia. Atmos. Res., 158, 192–209. http://dx.doi.org/10.1016/j.atmosres.2014.08.009.

Brewster, K., Hu, M., Xue, M., Gao, J., 2005. Efficient assimilation of radar data at high resolution for short-range numerical weather prediction. Extended Abstract, WWRP Int. Symp. Nowcasting Very Short Range Forecasting, Toulouse, France,

Météo-France, 3.06. [Available online at http://twister.ou.edu/papers/BrewsterWWRP_Nowcasting.pdf.]

Burgess, D.W., Donaldson Jr, R J., Desrochers, P.R., 1993. Tornado detection and warning by radar. The Tornado: Its structure, dynamics, prediction and hazards, Geophys. Monogr., No. 79, Amer. Geophys. Union, 203–221.

Burlando, M., Romanic, D., Solari, G., et al., 2017. Field data analysis and weather scenario of a downburst event in Livorno, Italy, on 1 October 2012. Mon. Weather Rev., 145, 3507–3527. https://doi.org/10.1175/MWR-D-17-0018.1

Carvalho, L.M.V., Jones, C., 2001. A satellite method to identify structural properties of mesoscale convective systems based on the maximum spatial correlation tracking technique (mascotte). J. Appl. Meteor., 40, 1683–1701. https://doi.org/ 10.1175/1520-0450(2001)040<1683:ASMTIS>2.0.CO;2

Clark, M.R., 2011. Doppler radar observations of mesovortices within a cool-season tornadic squall line over the UK. Atmos. Res. 100, 749–764. https://doi.org/ 10.1016/j.atmosres.2010.09.007

Clavner, M., Cotton, W. R., Heever, S. C., Saleeby, S. M., Pierce. J. R., 2018. The response of a simulated mesoscale convective system to increased aerosol pollution: Part I: Precipitation intensity, distribution, and efficiency. Atmos. Res., 199, 193–208. https://doi.org/ 10.1016/j.atmosres.2017.06.002

Comaniciu, D., Ramesh, V., Meer, P., 2003. Kernel-Based Object Tracking. IEEE Transactions on Pattern Analysis and Machine Intelligence, 25, 564–577.

Coniglio, M.C., Corfidi, S.F., Kain, J.S., 2010. Environment and early evolution of the

8 May 2009 derecho-producing convective system. Mon. Weather Rev., 139, 1083–1102. https://doi.org/10.1175/2010MWR3413.1

Ćurić M., Janc D., Vučković V., 2009. The influence of merging and individual storm splitting on mesoscale convective system formation. Atmos. Res., 93, 21–29. https://doi.org/10.1016/j.atmosres.2008.10.018

Davis, J.M., Parker, M.D., 2014. Radar climatology of tornadic and nontornadic vortices in high-shear, low-CAPE environments in the mid-Atlantic and Southeastern United States. Wea. Forecasting, 29, 828–853. https://doi.org/10.1175/WAF-D-13-00127.1

Dotzek, N., 2001. Tornadoes in Germany. Atmos. Res. 56, 233–251. https://doi.org/10.1016/S0169-8095(00)00075-2

Funk, T.W., et al., 1999. Storm reflectivity and mesocyclone evolution associated with the 15 April 1994 squall line over Kentucky and southern Indiana. Wea. Forecasting, 14, 976–993. https://doi.org/10.1175/1520-0434(1999)014<0976:sramea>2.0.co;2

Gander W, Golub G.H., Strebel, R., 1994. Least-squares fitting of circles and ellipses. BIT Numerical Mathematics, 34, 558–578. https://doi.org/10.1007/BF01934268

Gatzen, C., 2011. A 10-year climatology of cold-season narrow cold-frontal rainbands in Germany. Atmos. Res., 100, 366–370. https://doi.org/10.1016/j.atmosres.2010.09.018

Glickman, T.S., and Zenk, W., 2000. Glossary of Meteorology, 2nd edn. Amer. Meteor. Soc., 855 pp.

He, Z., Zhang, Q., Bai, L., Meng, Z.Y., 2017. Characteristics of mesoscale convective systems in central east china and their reliance on atmospheric circulation patterns. Int. J. Climatol., 37, 3276–3290. https://doi.org/ 10.1002/joc.4917

Johnson, J.T., Mackeen, P.L., Witt, A., Mitchell, E.D., Stumpf, G.J., Eilts, M.D., et al., 1998. The storm cell identification and tracking algorithm: An enhanced WSR-88D algorithm. Wea. Forecasting, 13, 263–276. https://doi.org/10.1029/2004rg000150

Lompar, M., Ćurić, M., Romanic D., 2017. Simulation of a severe convective storm using a numerical model with explicitly incorporated aerosols. Atmos. Res., 194, 164–177. https://doi.org/10.1016/j.atmosres.2017.04.037

Meng, Z.Y., Zhang, Y., 2012. On the squall lines preceding landfalling tropical cyclones in China. Mon. Weather Rev., 140, 445–470. https://doi.org/10.1175/MWR-D-10-05080.1

Meng, Z.Y., Yan, D., Zhang, Y., 2013. General features of squall lines in east china. Mon. Weather Rev., 141, 1629–1647. https://doi.org/10.1175/mwr-d-12-00208.1

Meng, Z.Y., Yao, D., Bai, L.q., et al., 2016. Wind estimation around the shipwreck of Oriental Star based on field damage surveys and radar observations, Sci. Bulletin, 61, 330-337. https://doi.org/10.1007/s11434-016-1005-2

Mitchell, E.D., Vasiloff, S.V., Stumpf, G.J., Witt, A., Eilts, M.D., Johonson, J.T., Thomas, K.W., 1998. The national severe storms laboratory tornado detection algorithm. Wea. Forecasting, 13, 352–366. https://doi.org/10.1175/1520-0434(1998)013<0352:tnsslt>2.0.co;2

Parker, M.D., Johnson, R.H., 2000. Organizational modes of midlatitude mesoscale convective systems. Mon. Weather Rev., 128, 3413–3436. https://doi.org/10.1175/1520-0493(2001)129<3413:OMOMMC>2.0.CO;2

Roberts, B. and M. Xue, 2017: The role of surface drag in mesocyclone intensification leading to tornadogenesis within an idealized supercell simulation. *J. Atmos. Sci*., 74, 3055–3077. https://doi.org/10.1175/JAS-D-16-0364.1

Rotunno, R., Klemp, J., 1985. On the rotation and propagation of simulated supercell thunderstorms. J. Atmos. Sci., 42, 271–292. https://doi.org/10.1175/1520-0469(1985)0422.0.CO;2

Schenkman, A. D. and Xue, M., 2016. Bow-echo mesovortices: A review. Atmos. Res., 170, 1–13. https://doi.org/ 10.1016/j.atmosres.2015.11.003

Schenkman, A.D., Xue, M., Shapiro, A., 2012. Tornado genesis in a simulated mesovortex within a mesoscale convective system. J. Atmos. Sci., 69, 3372–3390. https://doi.org/10.1175/JAS-D-12-038.1

Schenkman, A., Xue, M., Shapiro, A., Brewster, K., and Gao, J., 2011. Impact of CASA radar and Oklahoma mesonet data assimilation on the analysis and prediction of tornadic mesovortices in a MCS. Mon. Weather Rev., 139, 3422–3445. https://doi.org/10.1175/MWR-D-10-05051.1

Smith, T.M., Elmore K. L., 2004. The use of radial velocity derivatives to diagnose rotation and divergence. 11th Conf. on Aviation, Range, and Aerospace, Hyannis, MA, Amer. Meteor. Soc., P5.6. [Available online at http://ams.confex.com/ams/pdfpapers/81827.pdf.]

Trapp, R.J., Weisman, M. L., 2003. Low-level mesovortices within squall lines and bow echoes. Part II: Their genesis and implications. Mon. Weather Rev., 131, 2804–2823. https://doi.org/10.1175/1520-0493(2003)131<2804:lmwsla>2.0.co;2

Trapp, R.J., Stumpf, G.J., Manross, K.L., 2005a. A reassessment of the percentage of tornadic mesocyclones. Wea. Forecasting, 20, 680–687. https://doi.org/10.1175/WAF864.1

Trapp, R.J., Tessendorf, S.A., Godfrey, E.S., Brooks, H.E., 2005b. Tornadoes from squall lines and bow echoes. Part I: climatological distribution. Wea. Forecasting, 20, 23–34. https://doi.org/10.1175/waf-835.1

Thompson, R.L., Smith B.T., Dean A.R., Marsh P. T., 2014. Spatial distributions of tornadic near-storm environments by convective mode. Electronic J. Severe Storms Meteor., 8,1–22.

Wang, Y., Zheng, Y., Sun, K., and Wu, H., 2018: A statistical analysis of characteristics of mesocyclone products from Nanjing radar. Acta Meteorologica Sinica, 76, 266-278, doi: 10.11676/qxxb2017.08 (in Chinese)

Wapler, K., Hengstebeck, T., Groenemeijer P., 2016. Mesocyclones in Central Europe as seen by radar. Atmos. Res., 168, 112–120. https://doi.org/10.1016/j.atmosres.2015.08.023

Weisman, M.L., Trapp, R.J., 2003. Low-level mesovortices within squall lines and bow echoes. Part I: overview and dependence on environmental shear. Mon. Weather Rev., 131, 2779–2803. https://doi.org/10.1175/1520-0493(2003)131<2779:lmwsla>2.0.co;2

Xu, X., Xue, M., Wang Y., 2015a. Mesovortices within the 8 May 2009 bow echo over central United States: Analyses of the characteristics and evolution based on Doppler radar observations and a high-resolution model simulation. Mon. Weather Rev., 143, 2266–2290. https://doi.org/10.1175/mwr-d-14-00234.1

Xu, X., Xue, M., Wang, Y., 2015b. The genesis of mesovortices within a real data simulation of a bow echo system. J. Atmos. Sci., 72, 1963–1986. https://doi.org/10.1175/JAS-D-14-0209.1

Xu X., Xue M., Wang, Y., Huang, H., 2017. Mechanisms of secondary convection within a Mei-Yu frontal mesoscale convective system in eastern China. J. Geophys. Res., 122, 47–64. https://doi.org/10.1002/2016JD026017

Xue, M., Droegemeier, K.K., Wong, V., 2000. The Advanced Regional Prediction System (ARPS)—A multi-scale nonhydrostatic atmospheric simulation and prediction model. Part I: Model dynamics and verification. Meteor. Atmos. Phys., 75, 161–193. https://doi.org/10.1007/s007030070003

Xue, M., X. Luo, K. Zhu, Z. Sun, and J. Fei, 2018: The controlling role of boundary layer inertial oscillations in meiyu frontal precipitation and its diurnal cycles over China. *J. Geophy. Res*., 123, 5090–5115. https://doi.org/10.1029/2018JD028368

Zheng, L., Sun, J., Zhang, X., Liu, C., 2013. Organizational modes of Mesoscale Convective Systems over Central East China. Wea. Forecasting, 28, 1081–1098. https://doi.org/10.1175/WAF-D-12-00088.1

List of Tables

List of Figures

Fig. 6. Percentages of (a) maximum diameter (unit: km) and (b) maximum azimuthal shear (unit: 10^{-3} s^{-1}) for MVs of different lifetime.

Fig. 7. Percentage of the formation time of MCS-type MVs relative to the life cycle of parent MCSs.

Fig. 8. (a) Monthly variation, (b) diurnal variation (LST) and percentages of (c) maximum diameter (unit: km) and (d) maximum azimuthal shear (unit: 10^{-3} s^{-1}) for cell-MVs (blue bars) and MCS-MVs (red bars) in YHRB from April to July during 2013–2015.

Fig. 9. Composite environmental conditions in different months of 2013 through 2015. [(a), (b)] April–May and [(c), (d)] June–July. (e)-(h) are similar to (a)-(d) but for composite environmental conditions of different types of MVs. [(e), (f)] Cell-MVs and [(g), (h)] MCS-MVs. On the left panel, black and red contours are the 500 hPa geopotential height (units: m) and temperature (units: K), with the horizontal wind field denoted by vectors. The horizontal wind speed (units: m s^{-1}) at 200 hPa is shaded. On the right panel, black lines and vectors show the geopotential height (units: m) and horizontal wind at 850 hPa. The color shading in (b) (d) denotes the equivalent potential temperature (units: K) but horizontal wind speed in (f) (h). The gray shading denotes the terrain above 850 hPa. The green box indicates the location of YHRB.

Fig. 10. Composite [(a), (c)] CAPE (shading, units: J kg^{-1}) and water vapor flux at 700 hPa (vector) and [(b), (d)] vertical wind shear (shading and vector) in the layer of 1000–

700 hPa in different months of 2013 through 2015. [(a), (b)] April–May and [(c), (d)] June–July. (e)-(h) are similar to (a)-(d) but for different types of MVs. [(e), (f)] Cell-MVs and [(g), (h)] MCS-MVs. The green box indicates the location of YHRB.

Table 1. MVs detected at three radars from April to July during 2013–2015. Numbers in the parentheses are the percentages of MVs for different lifetime and parent systems.

	Wuhan	Hefei	Yancheng	Total
All MVs	1129	1875	786	3790
Short-lived	800 (71%)	1269 (68%)	542 (69%)	2611 (69%)
Moderate-lived	281 (25%)	500 (27%)	222 (28%)	1003 (26%)
Long-lived	48 (4%)	106 (5%)	22 (3%)	176 (5%)
MCS type	21 (2%)	261 (14%)	92 (12%)	374 (10%)
Cell type	1108 (98%)	1614 (86%)	694 (88%)	3416 (90%)

Table 2. Average diameter, azimuthal shear and lifetime of MVs detected at three radars in YHRB from April to July during 2013–2015

	Diameter (km)	Azimuthal shear (10^{-3} s^{-1})	Lifetime (min)
All MVs	8.1	2.3	26.3
Short-lived	7.6	2.2	20.1
Moderate-lived	9.2	2.4	36.2
Long-lived	10.2	2.7	61.5
MCS type	10.0	2.5	46.4
Cell type	6.0	2.1	24.0

Table 3. Average diameter, azimuthal shear and lifetime of MCS-type MVs detected at three radars in YHRB from April to July during 2013–2015

	Diameter (km)	Azimuthal shear (10^{-3} s^{-1})	Lifetime (min)
Short-lived	9.9	2.3	41.5
Long-lived	10.7	3.2	72.3

Table 4. Mean CAPE and vertical shear (between 1000 and 700 hPa) over YHRB averaged between 2013 and 2015

	April & May	June & July	Cell-type	MCS-type
CAPE (J kg^{-1})	36.4	384.5	275.2	333.0
$V_{1000\text{-}700}$ (m s^{-1})	5.7	4.3	5.0	6.5

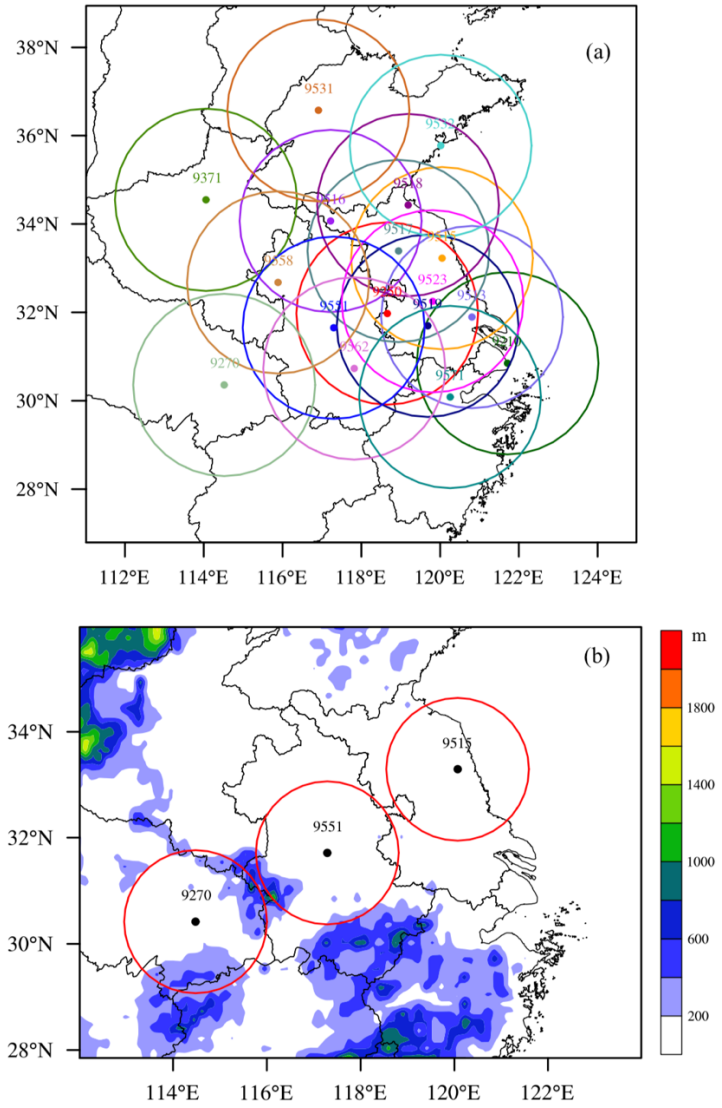

Fig. 1. (a) Location of 17 radars in YHRB including Nanhui (9210), Nanjing (9250), Wuhan (9270), Zhengzhou (9371), Nantong (9513), Yancheng (9515), Xuzhou (9516), Huaian (9517), Lianyungang (9518), Changzhou (9519), Taizhou (9523), Jinan (9531), Qingdao (9532), Hefei (9551), Fuyang (9558), Tongling (9562), and Hangzhou (9571). Color circles represent the 230 km range. (b) Location of Wuhan (9270), Hefei (9551) and Yancheng (9515) radars, with red circles denoting the 150 km range. Terrain heights are shaded (units: meter).

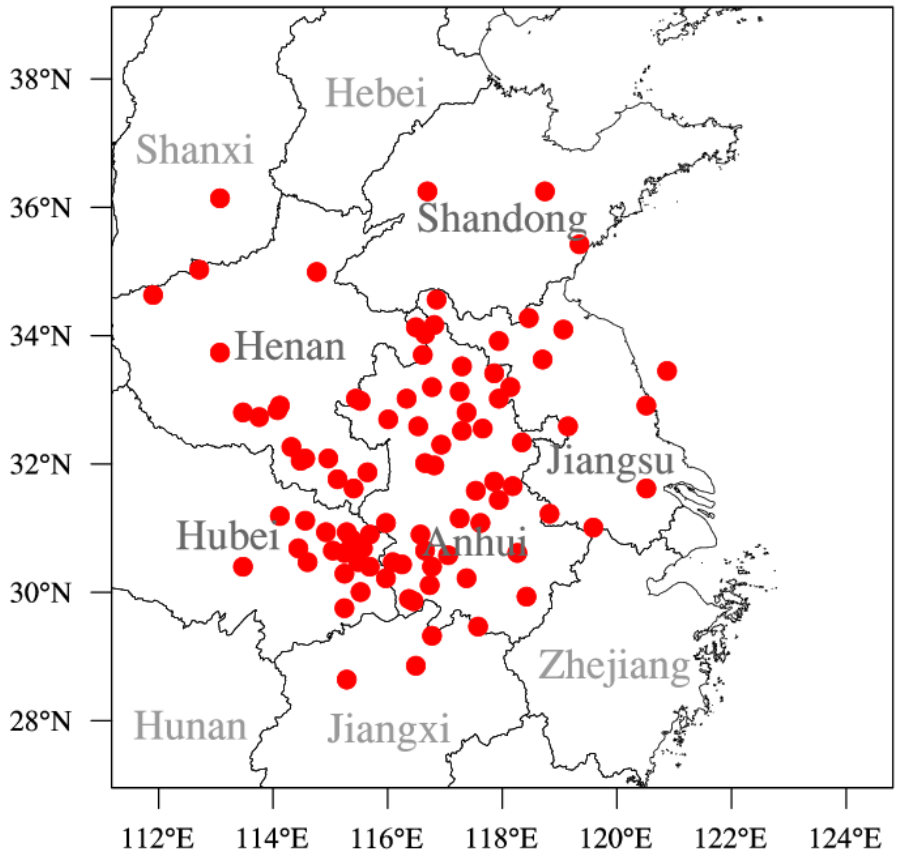

Fig. 2. Spatial distribution of the formation locations of MCSs in YHRB from April to July during 2013–2015.

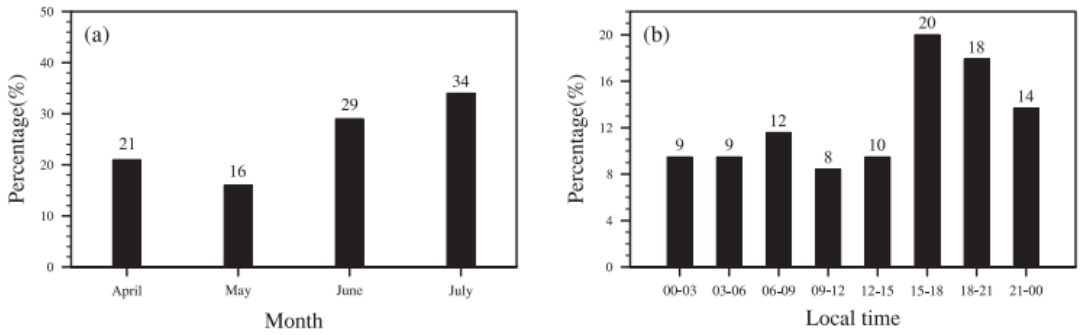

Fig. 3. (a) Monthly and (b) diurnal variations of MCSs in YHRB from April to July during 2013–2015.

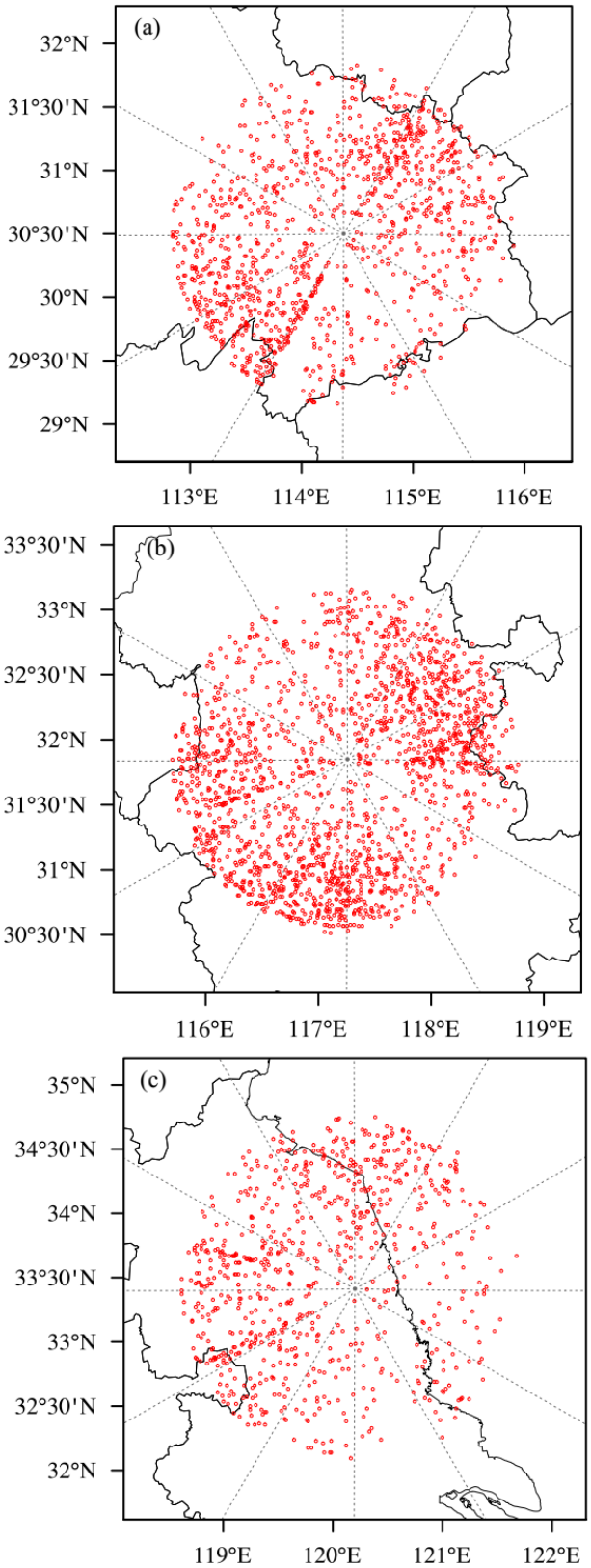

691

692 Fig. 4. Distributions of initial locations of MVs detected by radars of (a) Wuhan, (b)
693 Hefei, and (c) Yancheng from April to July during 2013–2015.

694

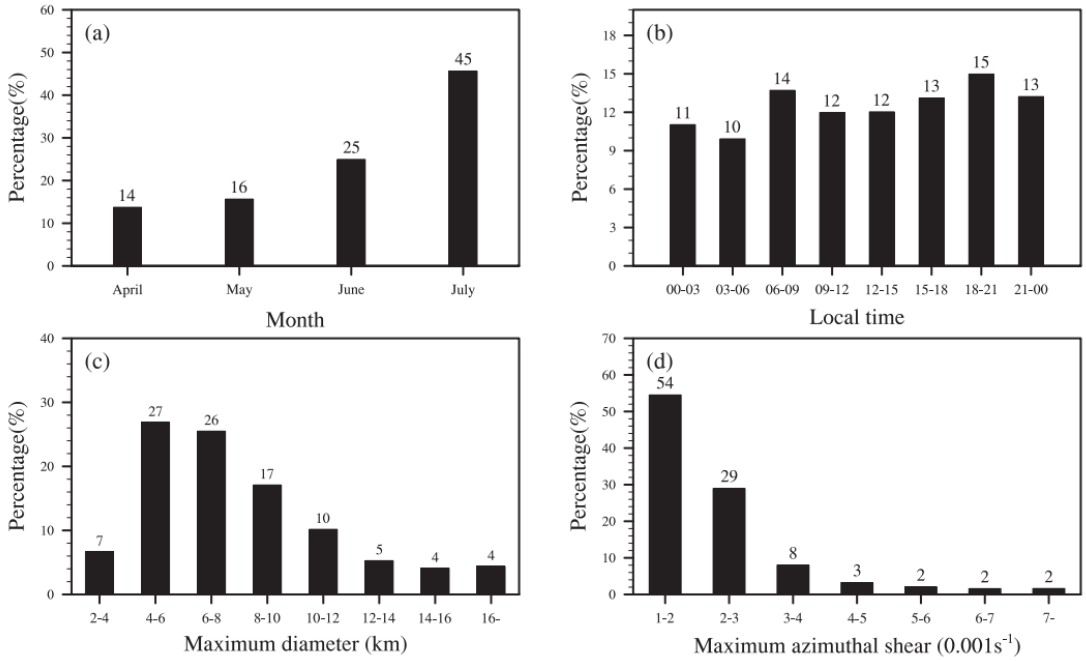

Fig. 5. (a) Monthly and (b) diurnal variations of MVs detected in YHRB from April to July during 2013–2015. (c) and (d) are the percentages of MV maximum diameter (unit: km) and maximum azimuthal shear (unit: 10^{-3} s^{-1}) during their lifetime.

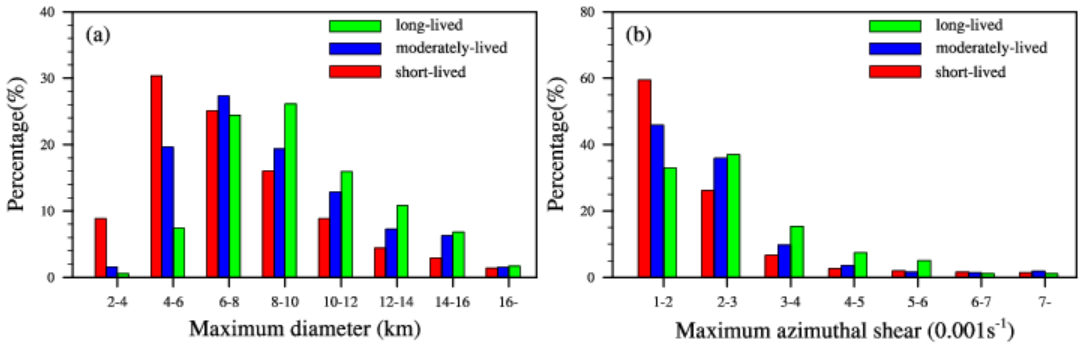

Fig. 6. Percentages of (a) maximum diameter (unit: km) and (b) maximum azimuthal shear (unit: 10^{-3} s^{-1}) for MVs of different lifetime.

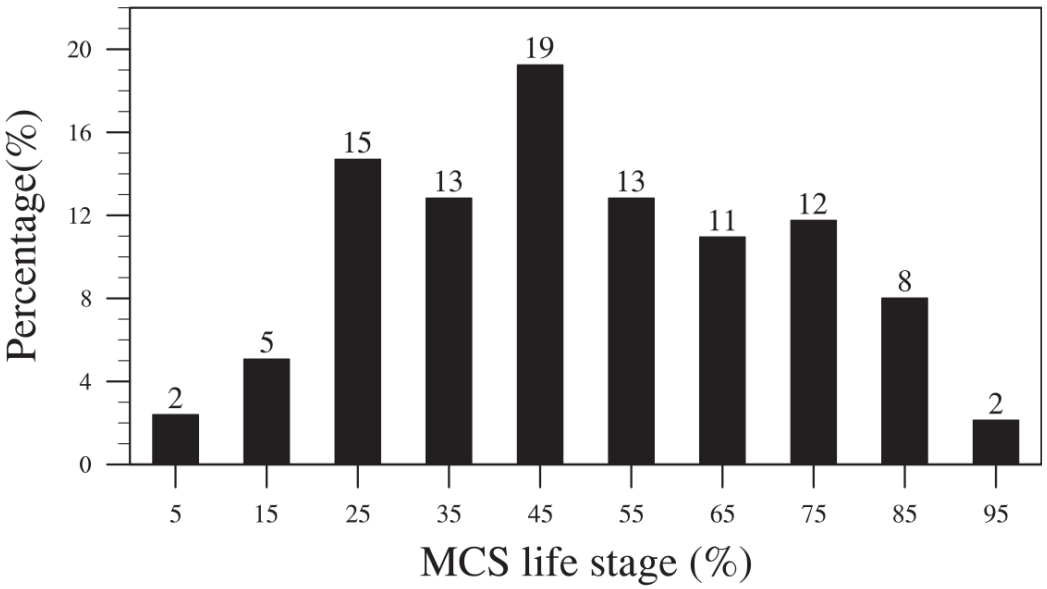

Fig. 7. Percentage of the formation time of MCS-type MVs relative to the life cycle of parent MCSs.

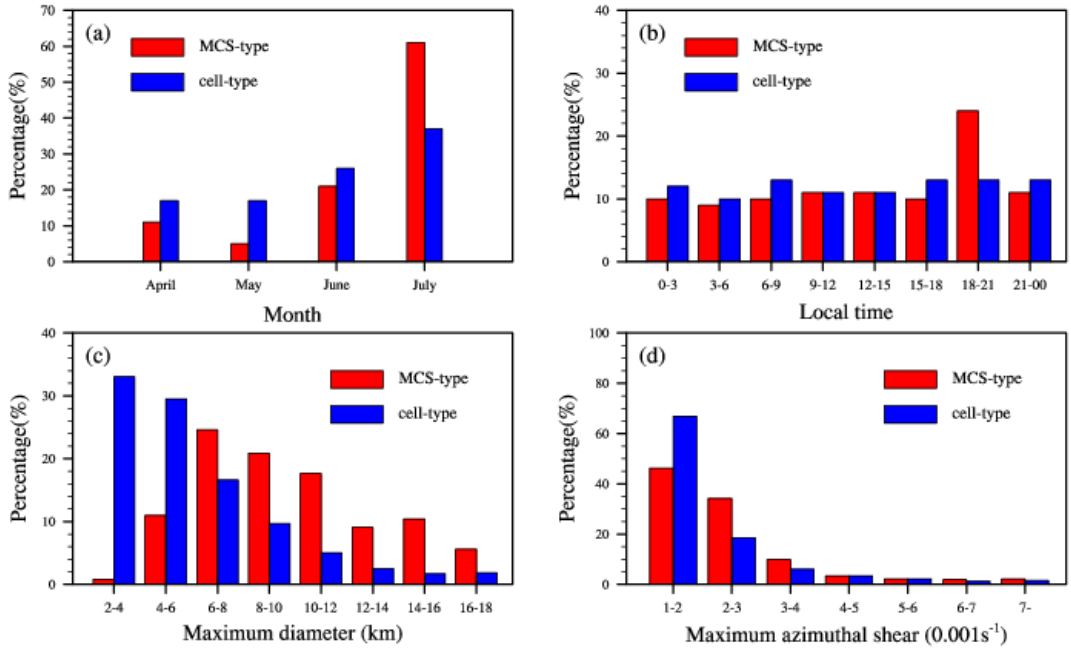

Fig. 8. (a) Monthly variation, (b) diurnal variation (LST) and percentages of (c) maximum diameter (unit: km) and (d) maximum azimuthal shear (unit: 10^{-3} s^{-1}) for cell-MVs (blue bars) and MCS-MVs (red bars) in YHRB from April to July during 2013–2015.

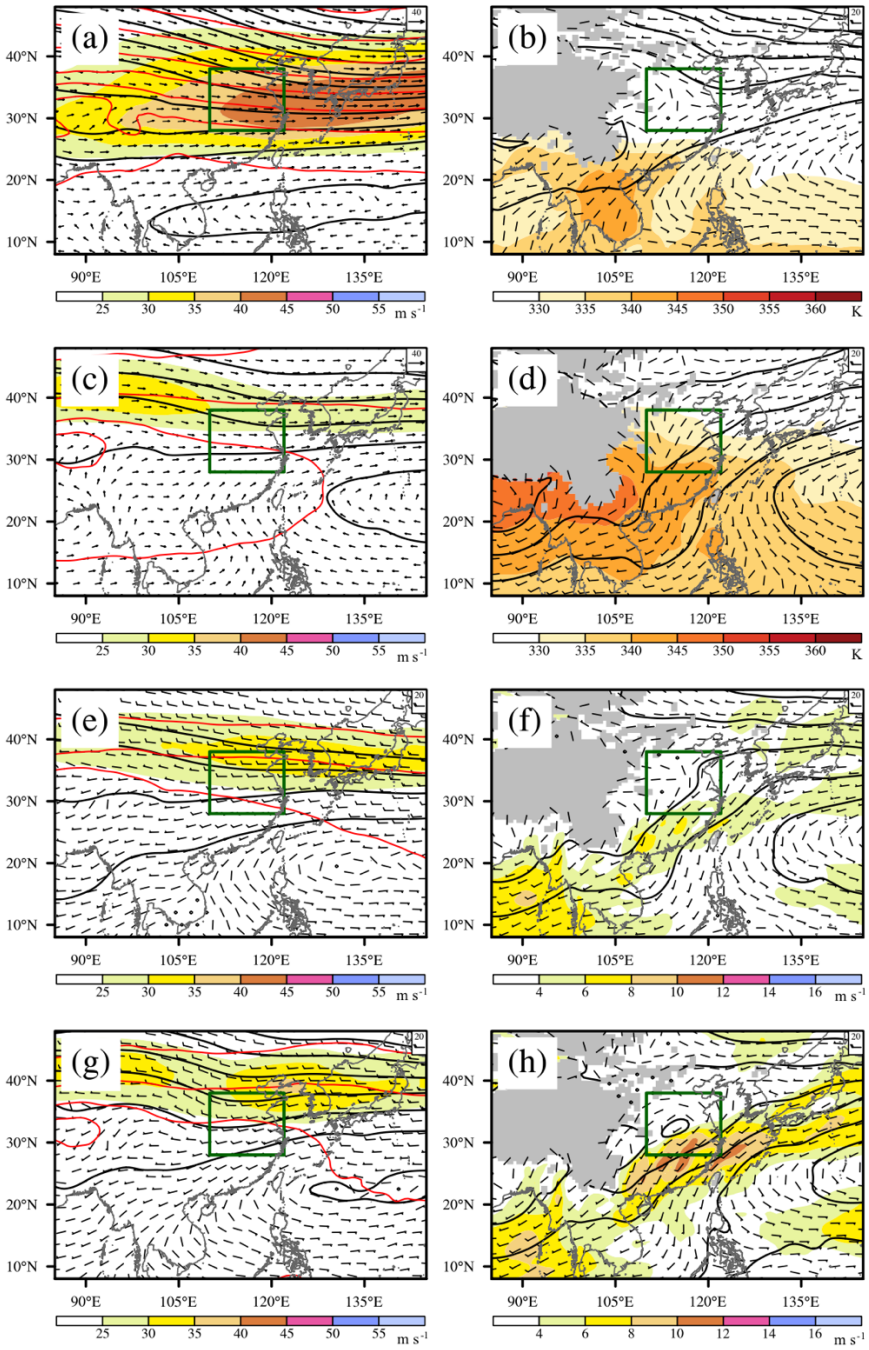

Fig. 9. Composite environmental conditions in different months of 2013 through 2015. [(a), (b)] April–May and [(c), (d)] June–July. (e)-(h) are similar to (a)-(d) but for composite environmental conditions of different types of MVs. [(e), (f)] Cell-MVs and [(g), (h)] MCS-MVs. On the left panel, black and red contours are the 500 hPa geopotential height (units: m) and temperature (units: K), with the horizontal wind field denoted by vectors. The horizontal wind speed (units: m s^{-1}) at 200 hPa is shaded. On the right panel, black lines and vectors show the geopotential height (units: m) and horizontal wind at 850 hPa. The color shading in (b) (d) denotes the equivalent potential temperature (units: K) but horizontal wind speed in (f) (h). The gray shading denotes the terrain above 850 hPa. The green box indicates the location of YHRB.

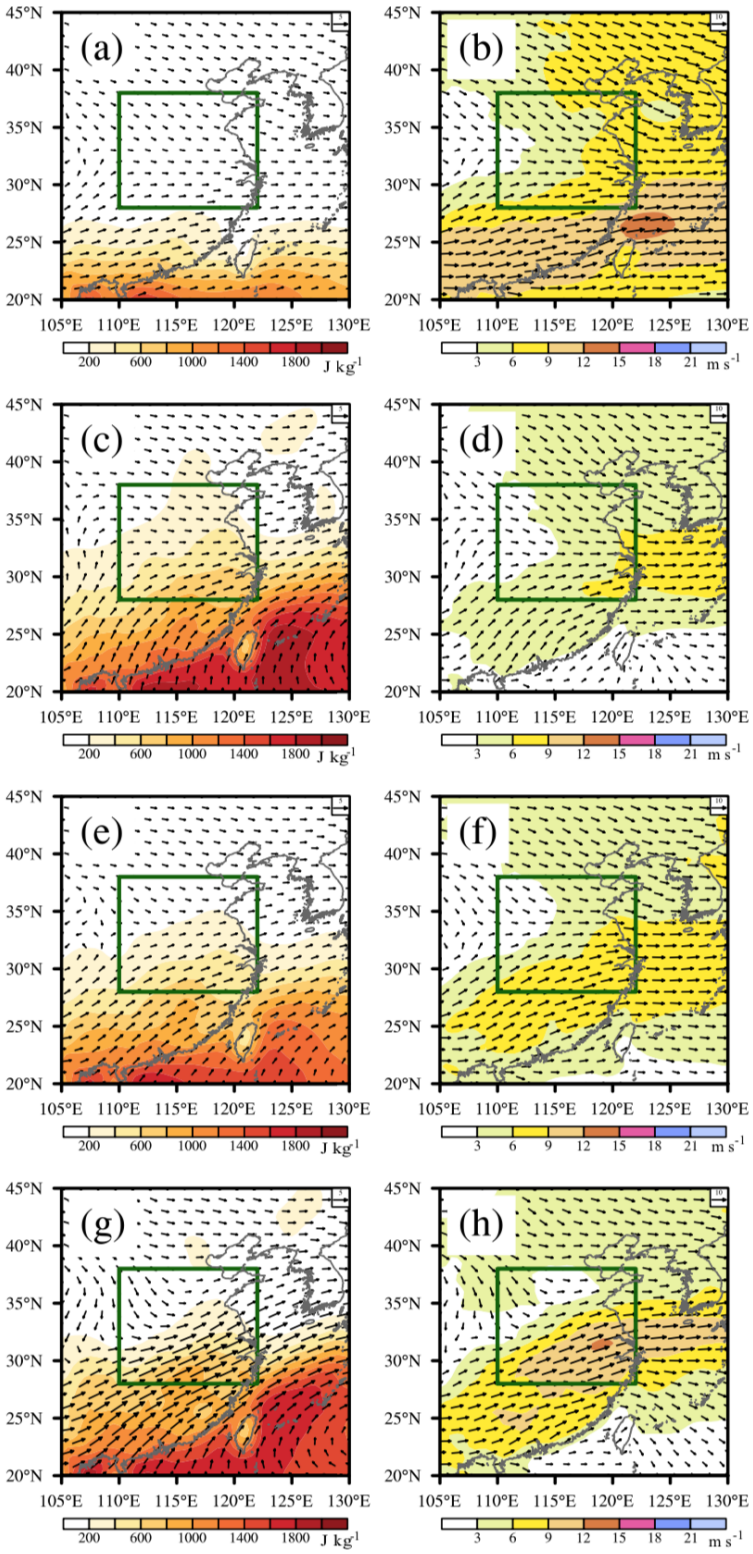

Fig. 10. Composite [(a), (c)] CAPE (shading, units: J kg^{-1}) and water vapor flux at 700 hPa (vector) and [(b), (d)] vertical wind shear (shading and vector) in the layer of 1000–700 hPa in different months of 2013 through 2015. [(a), (b)] April–May and [(c), (d)] June–July. (e)-(h) are similar to (a)-(d) but for different types of MVs. [(e), (f)] Cell-MVs and [(g), (h)] MCS-MVs. The green box indicates the location of YHRB.